Supplementary Information

S1. Device fabrication and measurement

The $NdTe_3$ were exfoliated utilizing Au-enhanced adhesion technique[1,2]. At first, the Si++/SiO_2 substrate was coated with 0.5/2.0 nm of Ti/Au by e-beam evaporation technique. Then, the wafer was transferred into an inert Argon environment of the glovebox without further explosion to the air. A freshly prepared surface of $NdTe_3$ was then pressed against the substrate. Large and uniform flakes of various thicknesses were selected for further device fabrication. Single crystals of *h*-BN were then exfoliated onto the surface of *Polydimethylsiloxane* (PDMS) and used to encapsulate the desired $NdTe_3$. A stamp consisting of PDMS/ *h*-BN was aligned above the $NdTe_3$ and then gently pressed until *h*-BN formed complete contact with the surface and afterward gradually released in a controlled manner. A few examples of resulting stacks are shown in Fig. S1a. Due to its environmental sensitivity, flake thicknesses of desired devices were identified by atomic force microscopy (AFM) after *h*-BN encapsulation Fig. S1b and c. The number of layers was counted starting from the bottommost layer of $NdTe_3$, which tends to cover a large area beneath the main channel flake and acts as a buffer layer. Interestingly note that a device based on this buffer layer alone shows insulating properties. Before device fabrication, the substrate resistance was inspected by the probe station to ensure the electrical insulation. The $NdTe_3$/*h*-BN stack was then covered with standard e-beam resist Poly(methyl methacrylate) (PMMA). Electrode regions were patterned with e-beam lithography and windows through *h*-BN were opened by the selective plasma etching process of the O_2+CF_4 mixture in the reactive ion etching (RIE) chamber. 0.5/50 nm of Ti/Au was deposited on top by an e-beam evaporator. Elevated temperatures were avoided throughout the complete fabrication process[3]. Afterward, the device was inserted into the cryostat and gradually cooled down to the base temperature. The transport measurement was performed using the standard AC lock-in technique (Stanford Research SR830 at 13 Hz) in the four-probe configuration.

S2. Carrier concentration and Fermi surfaces

Hall effect measurement and two-band model

To estimate transport mobilities and carrier concentration we perform a Hall effect measurement Fig. S2 a. Here, $\rho_{xy} = \frac{\rho_{xy}(B)-\rho_{xy}(-B)}{2}$ is an anti-symmetrized component of transverse resistivity ρ_{xy}. Assuming a two-band model, Hall effect resistivity can be expressed as follows

$$\rho_{xy}(B) = \frac{B}{e} \cdot \frac{(n_h {\mu_h}^2 - n_e {\mu_e}^2) + (n_h - n_e)(\mu_h \mu_e B)^2}{(n_h \mu_h + n_e \mu_e)^2 + (n_h - n_e)^2 (\mu_h \mu_e B)^2} \qquad (1)$$

where e is an electron charge, n_e and n_e are electron and hole concentration, μ_e and μ_h are electron and hole mobilities. Here, zero-field longitudinal resistivity is defined from the conductivity contribution of two parallel channels as

$$\rho_{xx}^0 = \frac{1}{e} \cdot \frac{1}{n_e \mu_e + n_h \mu_h} \qquad (2)$$

and a slope of the Hall resistivity in the high field limit expressed through the carrier difference as

$$\rho'_{xy} = \left. \frac{\partial \rho_{xy}}{\partial B} \right|_{B \to large} = \frac{1}{e} \cdot \frac{1}{n_h - n_e} \qquad (3)$$

Considering the constraints (2) and (3), two-band Hall resistance (1) can be written as

$$\rho_{xy}(B) = B \cdot \frac{\frac{\mu_h - \mu_e}{\rho_{xx}^0} + \frac{\mu_h \mu_e}{\rho'_{xy}} + \frac{(\mu_h \mu_e B)^2}{\rho'_{xy}}}{\left(\frac{1}{\rho_{xx}^0}\right)^2 + \left(\frac{\mu_h \mu_e B}{\rho'_{xy}}\right)^2} \qquad (4)$$

, and therefore reducing the number of adjustable parameters to μ_h and μ_e. Here, ρ_{xx}^0 and ρ'_{xx} can be deduced from the experiment Fig. S2 b. It is worth noting that $NdTe_3$ is a multiband system, therefore two-band model gives only a rough estimate of the carrier concentration in the system. On the other hand, including more bands into a fitting expression increases fitting uncertainty due to incrementing number of unconstrained parameters.

Fermi surface area and carrier concentration deduced from SdH oscillations

The correspondence between the oscillation frequency in Teslas – f, and the cross-sectional area of the Fermi surface S_F are linked via Onsager relation $f = \frac{\phi_0}{2\pi^2} S_F$, where ϕ_0 is fundamental flux quantum. The relative Fermi surface cross-sectional area ratio S_F / A_{BZ} for $\alpha_{1,2}, \beta_{1,2}, \gamma_{1,2}, \eta_{1,2}$ oscillations that were observed in SdH effect correspond to 0.19%, 0.21%, 2.18%, 2.31%, 3.83%, 4.05%, 8.43%, and 9.41% of the Brillouin zone area, where $A_{BZ} = 2.09$ Å^{-2} was used[4].

An alternative way to estimate a carrier density from the FS pocket determined by SdH oscillation is from Luttinger's theorem. The carrier density n is related to the D dimensional FS volume in k space as

$$n = 2 \int_{G(\omega=0,p)>0} \frac{d^D k}{(2\pi)^D} \qquad (5)$$

, where $G(\omega = 0, p)$ is a single-particle Green function of frequency and momentum. In the simple case of 2-dimensional spherical FS with no dispersion in k_Z direction eq(5) reduces to

$$n_{2D} = N_v N_s \frac{2S_F}{(2\pi)^2} = N_v N_s \frac{f}{\phi_0} \qquad (6)$$

, where N_v and N_s are valley and spin degeneracy factors. Estimated carrier concentrations deduced from eq(6) are presented in Table S2.

The total carrier concentration is then summed up to $n_{2D}^{tot} = \sum_{i=\alpha..\delta} n_{2D}^{f_i} = 9.34 \cdot 10^{14} cm^{-2}$, where i is an FS index. Considering the total carrier concentration obtained from the Hall effect measurements Fig. S2d as $n_{2D}^{Hall} = 16.5 \cdot 10^{14} cm^{-2}$, we can find that the resulting discrepancy between Hall carrier density and carrier density extracted from SdH oscillations $n_{2D} = n_{2D}^{Hall} - n_{2D}^{tot}$ can be ascribed to a 4-fold degenerate pocket with an average frequency of $\langle f \rangle = 3.71\ kT$. Despite the absence of respective SdH oscillations in this range, de Haas-van Alphen revealed two peaks in this range with $f_1 = 3.62\ kT$ and $f_2 = 3.83\ kT$.

S3. Two component Lifshitz-Kosevich fit.

Traces of the temperature evolution of the oscillatory component of resistivity $\Delta\rho_{osc}(1/B\ ,T)$ measured from different samples are shown in Fig. S3. Magnetic field orientation was fixed perpendicular to the layers throughout the measurement. Here, we used a two-component L-K expression to find the best fit to the base temperature envelope

$$\frac{\Delta\rho_{\mathrm{osc}}}{\rho_0} = A_1 \exp\left(\frac{-\pi}{B\mu_{q1}}\right) sin\left(2\pi\left(\frac{f_1}{B} - \varphi_1\right)\right) + A_2 \exp\left(\frac{-\pi}{B\mu_{q2}}\right) sin\left(2\pi\left(\frac{f_2}{B} - \varphi_2\right)\right) \qquad (7)$$

, where A, μ_q, f and φ are adjustable parameters responsible for the overall amplitude, amplitude decay in $1/B$, the oscillating period in $1/B,$ and phase offset respectively. The corresponding oscillatory traces extracted from various samples are shown in Fig. S4. An example of fiting an individual oscillatory components is shown in Fig. S5 a. Fitting parameters can be found in Table S1. The extraction of the phase factor is complicated due to Zeeman splitting and smearing effects, therefore not presented in this work.

S4. Band structure calculations

The electronic structure of $NdTe_3$ was calculated within the GGA+U approximation[6,7] Fig. S8, as implemented in the VASP code for bulk, monolayer and bilayer in the antiferromagnetically (AFM) ordered phase between nearest-neighbour Nd atoms Fig. S8. The on-site Coulomb parameter for the Nb f-states, U = 9.26 eV, and J = 0.45 eV, were determined from cRPA calculations[8-11]. Conventional unit cell was utilized with the unit cell vectors (in Å units) $\boldsymbol{a} = (4.39, 0, 0)$, $\boldsymbol{b} = (0, 26.9, 0)$ and $\boldsymbol{c} = (0, 0, 4.39)$. Brillouin zone sampling employed a $12 \times 2 \times 12$ k-point mesh for the bulk and $12 \times 1 \times 12$ k-points for the monolayers. The primary objective of using DFT is to quantitatively investigate the impact of thickness on electronic structure of $NdTe_3$. Our electronic structure calculations of the monolayer, bilayer, and bulk films shows minor impact on the dispersion near the Fermi level.

S5. Data processing protocol

The data obtained throughout this work was batch analyzed by the algorithm schematically depicted in Fig. S9. Measured magnetoresistivity $\rho(B)$ was first plotted vs inverse magnetic field $\rho(1/B)$ and differentiated with respect to $1/B$. The latter is aimed to lower the order of the polynomial background of smoothly varying classical magnetoresistance while preserving information about the oscillatory component. The data were then interpolated over a specific inverse magnetic field range and smooth background subtracted. The resulting signal was then used to obtain Fast-Fourier Transform spectra. Alternatively, a defined integral was taken to recover an amplitude of the oscillatory component of the signal $\Delta\rho_{\mathrm{osc}}(1/B)$.

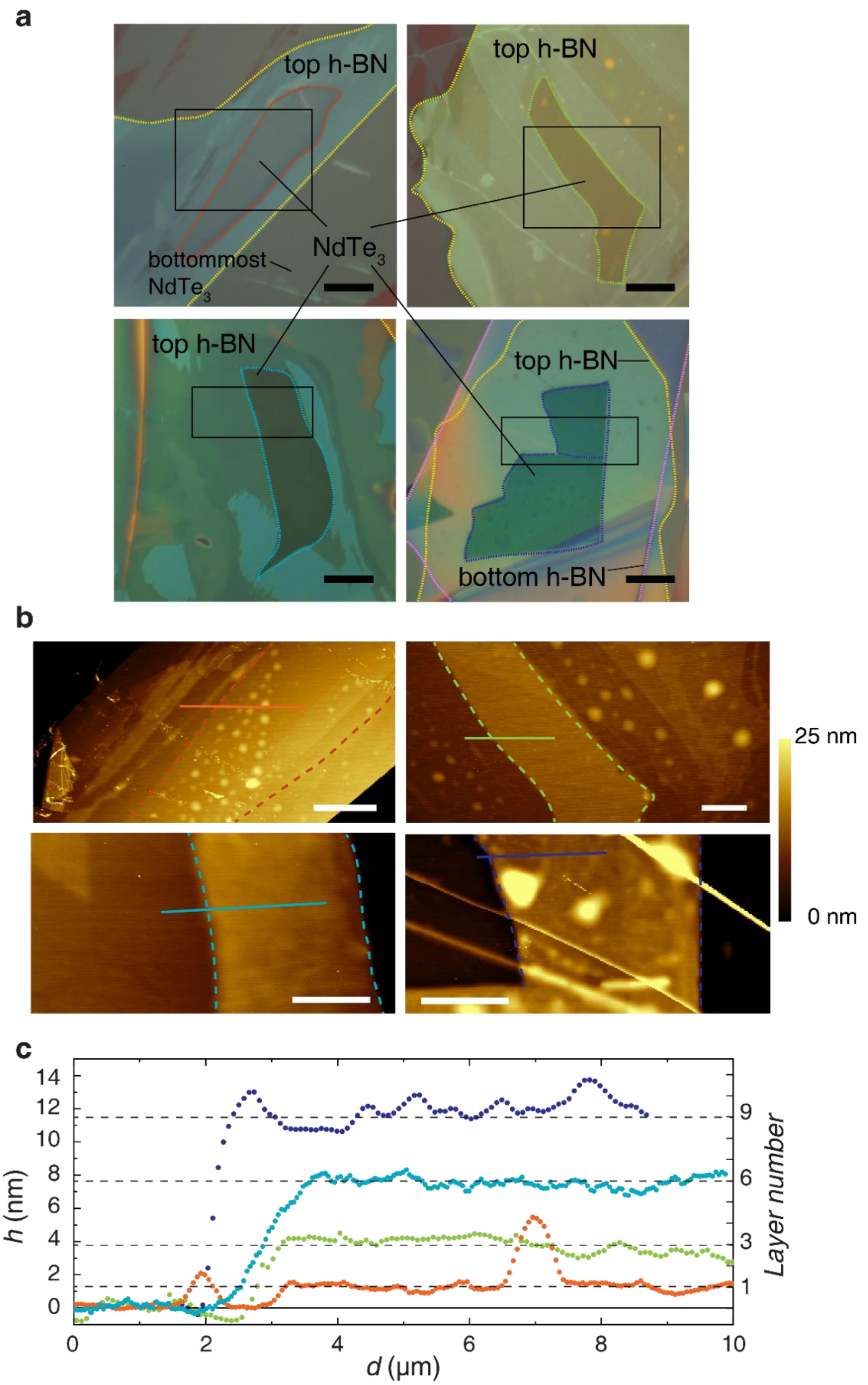

Fig. S1 Layer identification and surface morphology characterization. a, Optical micrographs of $NdTe_3$ flakes with the *h*-BN encapsulation. Inner dotted contour highlights the area later used for the device channel. The outer dotted line marks the boundary of the *h*-BN flake. The scale bar is 10 µm. **b,** Atomic force microscopy images of the flakes in **a.** Scalebar is 5 µm. **c,** AFM profiles extracted along the solid lines in **b**. The same color scheme as in **a.** and **b.** is used. Step height corresponding to 1 layer is identified to be ~1.3 nm. A layer number is counted starting from the bottommost discontinuous layer of $NdTe_3$.

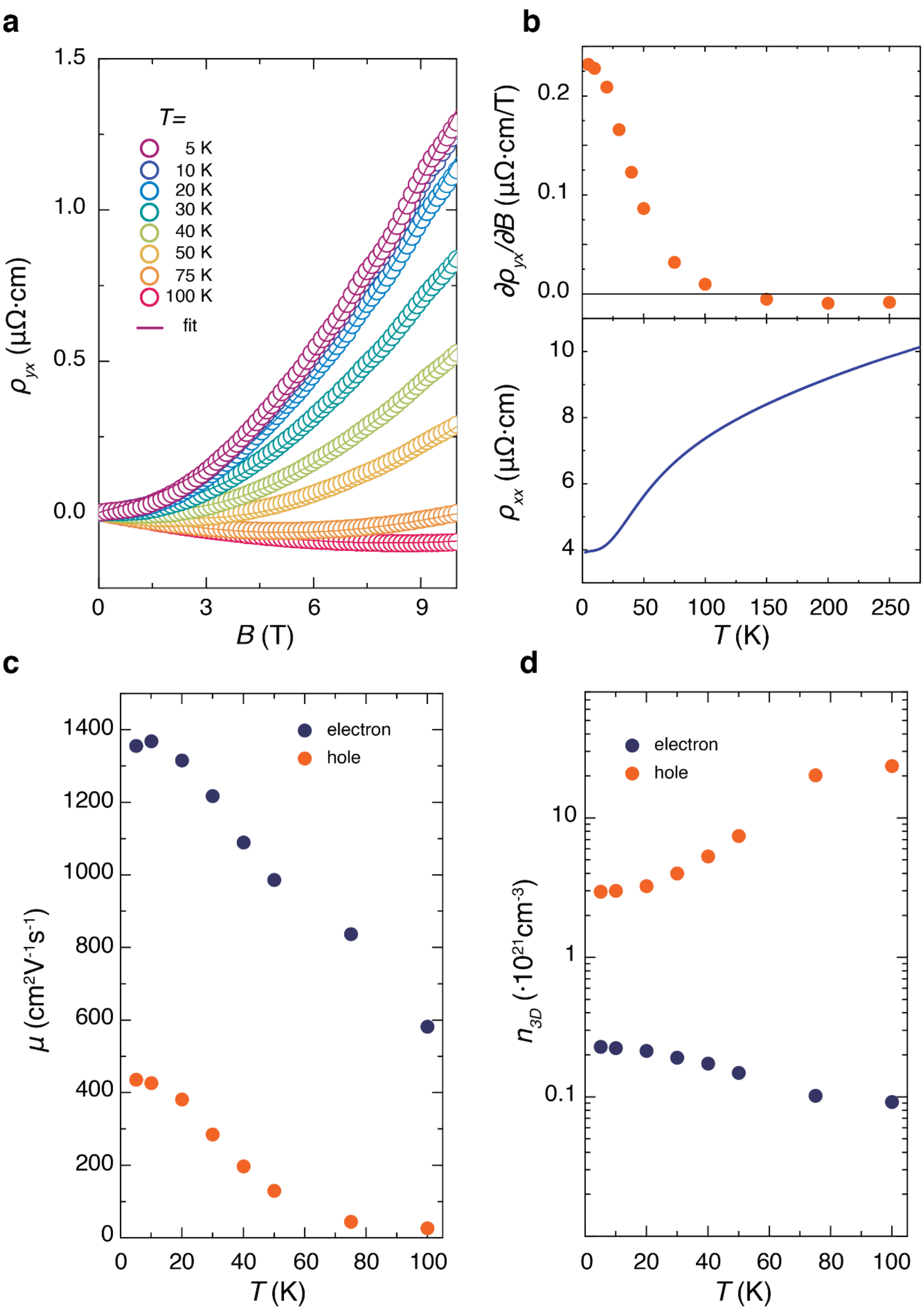

Fig. S2 Hall effect measurement for determining the carrier density and mobility. a, Symmetric component of Hall resistivity of 4 layer sample at different temperatures. Solid lines are two carrier model fits of Hall resistivity data. **b,** High-field slope of the Hall resistivity (upper panel) and longitudinal resistivity (lower panel) vs. temperature. **c,** The **t**emperature dependence of electron and hole mobilities extracted from two carrier model fitting. **d,** Electron and hole concentrations at different temperatures obtained by two carrier model fit.

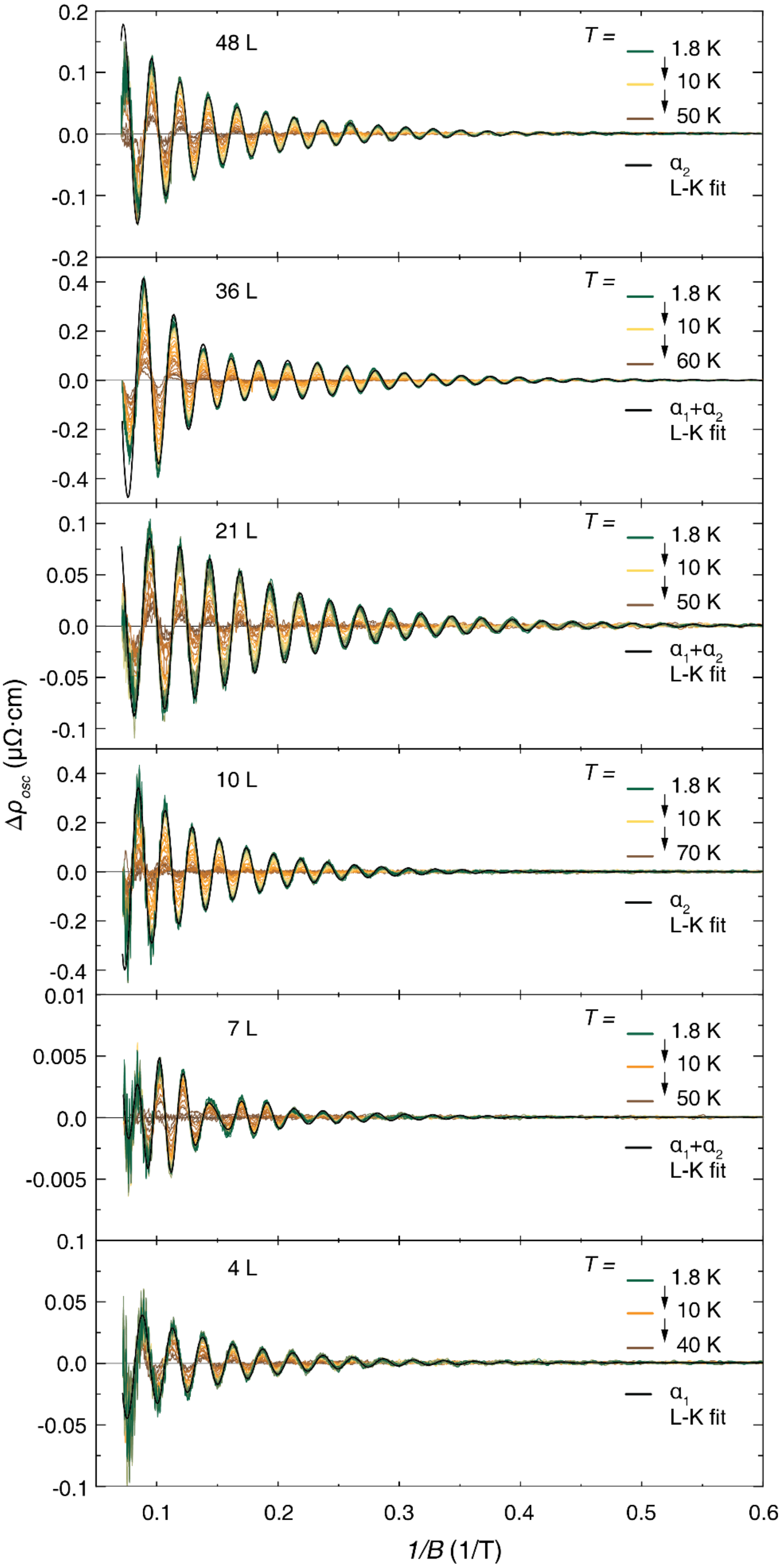

Fig. S3 Thermal damping of SdH oscillations. Temperature evolution of resistivity oscillations plotted against the inverse magnetic field for different sample thicknesses. The solid line is the Lifshitz-Kosevich fit of 1.8 Kelvin data.

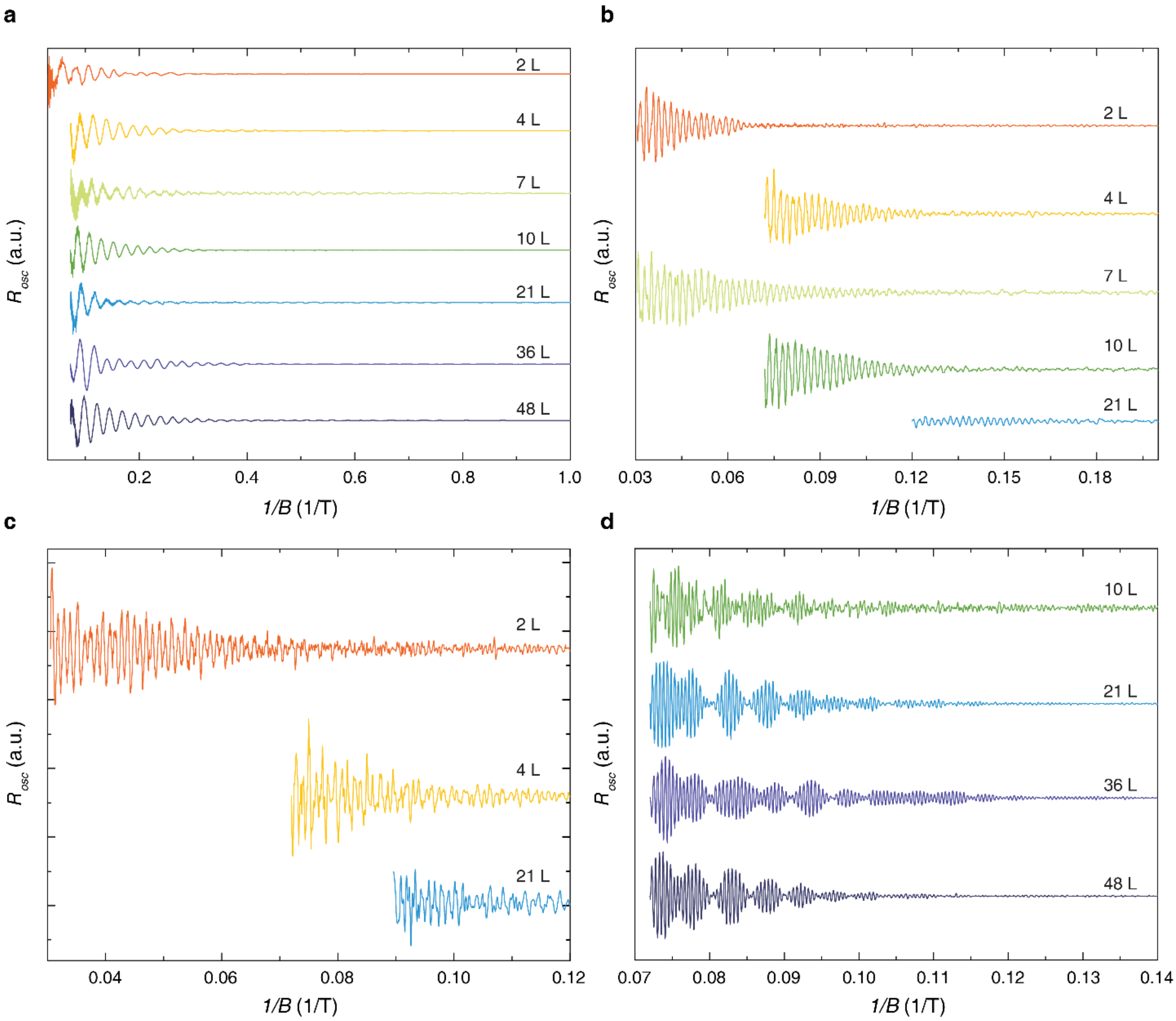

Fig. S4. Oscillating components. A comprehensive overview of the normalized oscillating signal corresponding **a,** $\alpha -$ pocket, **b,** $\beta -$ pocket, **c,** $\gamma -$ pocket and **d,** $\eta -$ pocket obtained from different sample thicknesses.

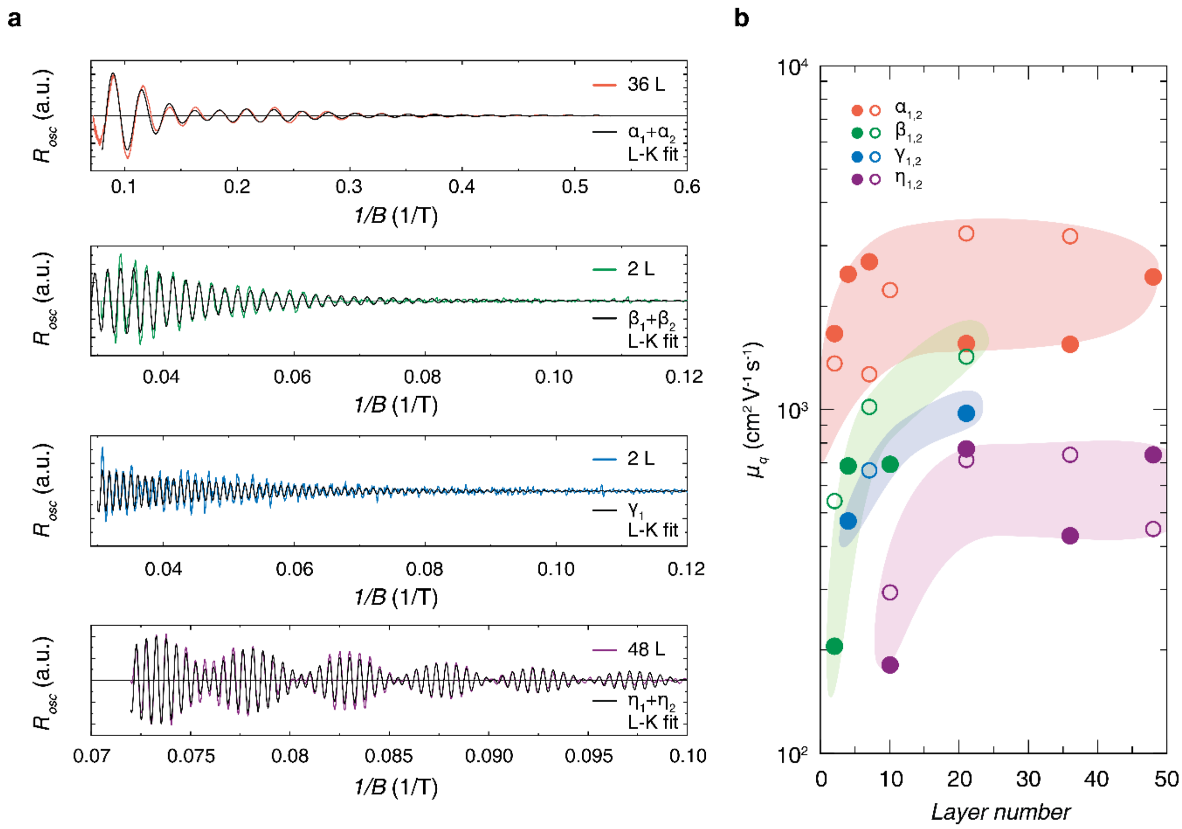

Fig. S5. Quantum mobility reduction. a, Example of Lifshitz-Kosevich fit of principal oscillatory frequencies observed in different samples. . **b,** Quantum mobility extracted from the L-K fit plotted vs layer number obtained from all measured samples.

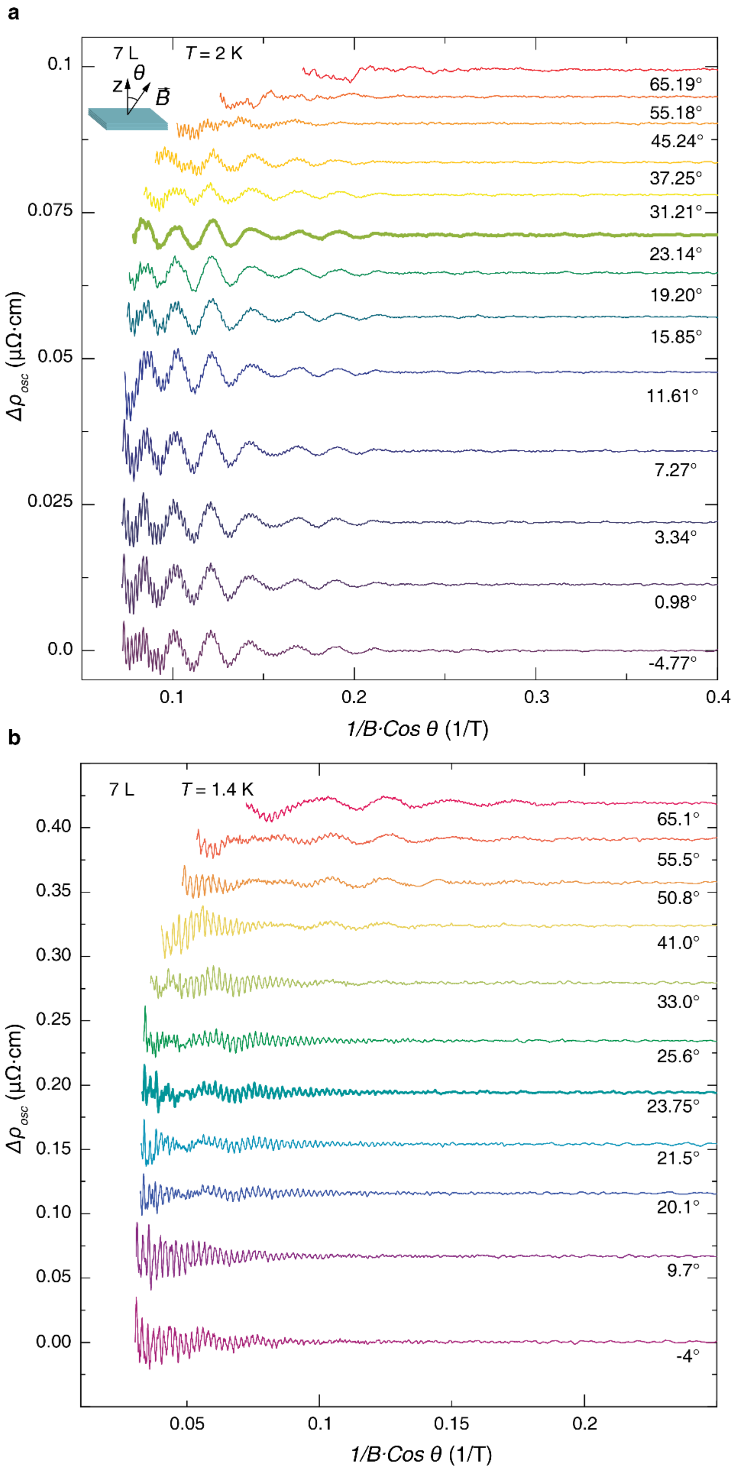

Fig. S6 Spin damping in a tilted field. a, Oscillatory component of resistivity extracted from 7 layer sample plotted vs perpendicular component of inverse magnetic field $\Delta\rho_{osc}(1/B\,,\theta)$ for different out-of-plane angle θ. Trace corresponding to zero spin state of fast oscillating β pocket close to 23.1° is highlighted by a thicker line. **b,** Oscillatory traces of another 7L sample measured up to 33 T shows considerable amplitude damping at ~23.8°.

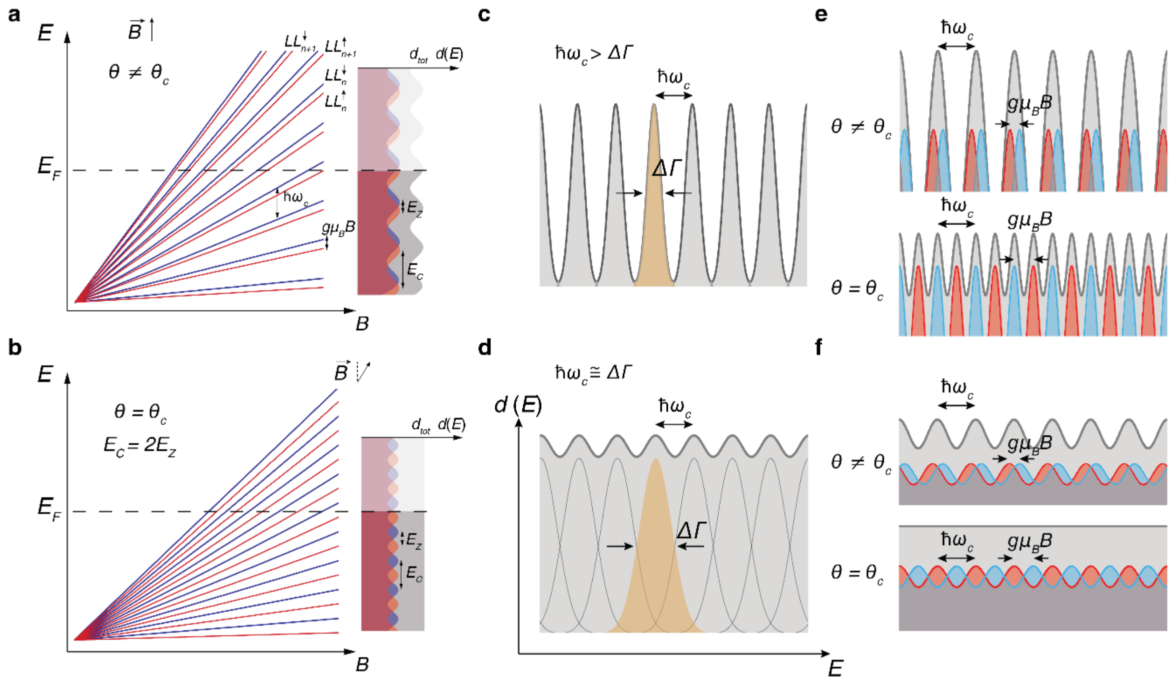

Fig. S7. Zero spin and Landau Level broadening. a, Schematics of the Landau Levels formed in a single band under applied perpendicular magnetic field including spin-splitting. Here, cyclotron energy E_C is much larger than Zeeman splitting E_Z. Fermi level E_F is marked by the dashed line. *Right panel:* density of spin-up, spin-down, and resulting states are depicted by blue, red, and grey respectively. **b,** Landau Levels formed under a tilted magnetic field at the critical angle θ_C, where $E_C = 2E_Z$. **c,** Schematic picture of the density of states of well-separated $\hbar\omega_c > \Delta\Gamma$ and **d,** highly broadened $\hbar\omega_c \cong \Delta\Gamma$ Landau Levels. **e,** Density of states of well-separated Landau Levels in a presence of Zeeman splitting away from the critical angle (*upper panel*) and at the critical angle (*lower panel*). Modulation of total *dos* doubles the frequency at a critical angle. **f,** Density of states of broadened Landau Levels in a presence of Zeeman splitting away from a critical angle (*upper panel*) and close to a critical angle (*lower panel*). Modulation of total *dos* vanishes at a critical angle.

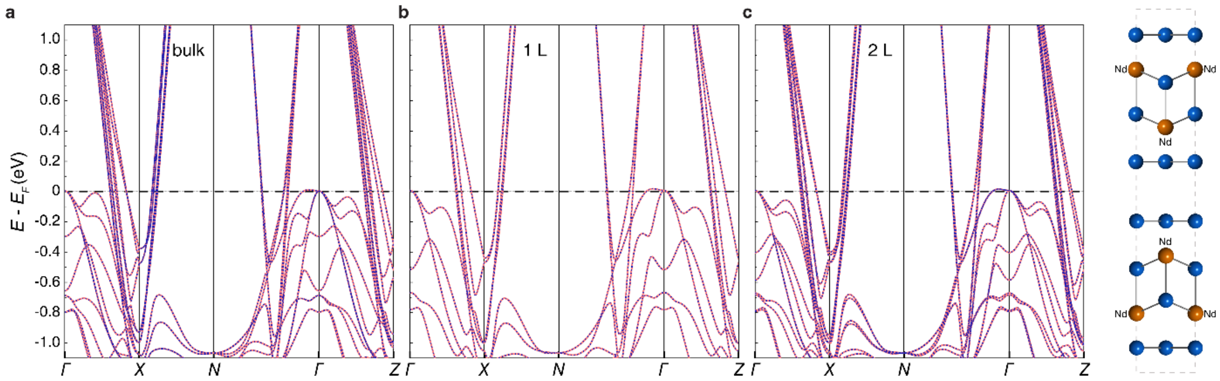

Fig. S8. Calculated band structure of $NdTe_3$. Electronic structure of **a,** bulk **b,** monolayer and **c,** bilayer $NdTe_3$ in AFM phase. Schematic crystal structure of the $NdTe_3$ unit cell is shown in the right.

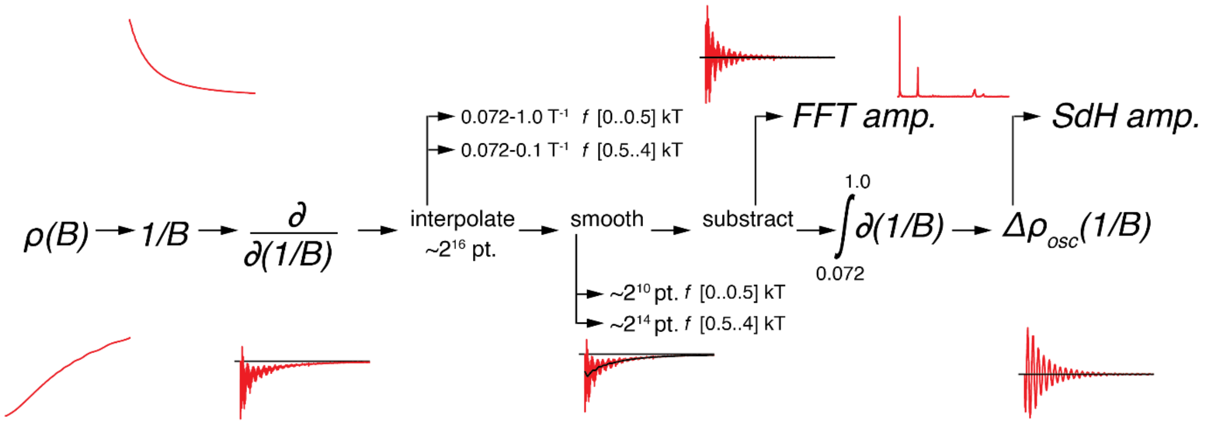

Fig. S9 Data processing protocol. Step-by-step (from left to right) data treatment was used in the present study for the extraction of various quantum oscillatory parameters. Real data example obtained after each step is shown by red trace. The zero-level position is marked by a black straight line.

Table S1. Parameters extracted from L-K analysis of SdH oscillations including observed oscillation frequencies f, a corresponding 2D carrier concentration n_{2D}, Dingle temperature T_D, quantum mobility μ_q and cyclotron mass ratio m^*/m_e. Numbers without any label are extracted from FFT analysis; () – denote data extracted from an analysis of the envelope of SdH oscillations; * data observed in high magnetic fields; † parameters extracted from zero spin effect.

FS pocket	*Layer number*	f (T)	$n_{2D} \cdot 10^{13}$ (cm^{-2})	T_D (K)	μ_q $(cm^2V^{-1}s^{-1})$	$\frac{m^*}{m_e}$
α_1	48	--	--	--	--	--
	36	34.5 (35.5)	0.16 (0.17)	--	(1551) 925†	--
	21	39.8 (40)	0.19 (0.19)	(19.9)	(1558)	(0.069) 0.083
	10	--	--	--	--	--
	7	45.2 (44)	0.22 (0.21)	(25.2)	(1116)	(0.076) 0.080
	4	38.8 (40.2)	0.19 (0.19)	(12.5) 3.2†	(2480) 8928†	(0.069) 0.074
	2	39-55*	0.19-0.26	--	--	--
α_2	48	43 (43.1)	0.21 (0.21)	(13)	(2937)	(0.056) 0.079
	36	42 (41.9)	0.20 (0.20)	(10.3)	(3193)	(0.065) 0.068
	21	-- (44)	-- (0.21)	--	(3260)	--
	10	44.2 (45)	0.21 (0.22)	(12.3) 9.7†	(2230) 2272†	(0.078) 0.097
	7	57 (57.3)	0.27 (0.28)	--	(2651)	--
	4	--	--	--	--	--
β_1	48	474	2.29	--	--	-- 0.29
	36	--	--	--	--	--
	21	487(493)	2.35	(5.2)	(1425)	-- 0.29
	10	487(481)	2.35	16.8†	(693)444†	-- 0.29
	7	483(479)	2.33	7.1†	(1030)1429†	-- 0.21
	4	480(479)	2.32	8.6†	(687)854†	-- 0.29
	2	468*(468)	2.26	--	(205)	--
β_2	48	508	2.46	--	--	-- 0.29
	36	--	--	--	--	--
	21	501	2.42	--	--	-- 0.29
	10	--	--	--	--	--
	7	--	--	--	--	--
	4	--	--	--	--	--
	2	506*(506)	2.4	--	(543)	--
γ_1	48	826	3.99	--	--	-- 0.39
	36	848	4.07	--	--	-- 0.33
	21	840(840)	4.06	(4.1)	(975)	-- 0.53
	10	849	--	12.3†	598†	-- 0.29
	7	--	--	--	--	--
	4	--	--	--	--	--
γ_2	48	860	4.16	--	--	-- 0.34
	36	877	4.24	--	--	--
	21	872	4.22	--	--	--
	10	--	--	--	--	--
	7	910*(918)	4.42	(7.8)3.5†	(667)1492†	-- 0.41
	4	887 (895)	4.29	6.2†	882†	-- 0.39
η_1	48	1848(1848)	8.94	(5.4)	(739)	-- 0.54
	36	1843(1843)	8.92	(9.9)	(431)	-- 0.50
	21	1831(1839)	8.86	(2.8)	(1474)	-- 0.51
	10	1837-1872(1841)	8.9-9.1	(21.5)	(181)	-- 0.55
	7	--	--	--	--	--
	4	--	--	--	--	-- 0.61
η_2	48	2057(2057)	9.95	(7.6)	(450)	-- 0.63
	36	2052(2052)	9.92	(4.4)	(739)	-- 0.66
	21	2060(2053)	9.96	(8.2)	(420)	-- 0.62
	10	2050-2080(2069)	9.92-10.1	(10.7)	(294)	-- 0.68
	7	--	--	--	--	--
	4	--	--	--	--	--

Table S2. Estimated parameters for unobserved pocket η deduced from the mean frequencies $\langle f \rangle$ of observed pockets and total carrier density measured by the Hall effect n_{2D}^{Hall}. Spin N_s and valley N_v degeneracy were included.

Fermi pocket	$\langle \boldsymbol{f} \rangle$ $(\boldsymbol{T})$	$\boldsymbol{N_v}$	$\boldsymbol{N_s}$	$\boldsymbol{n_{2D} \times 10^{14}}$ $(\boldsymbol{cm^{-2}})$	$\boldsymbol{S_F}$ $\boldsymbol{/A_{BZ}}$
$\boldsymbol{\alpha_1}$	41.2	4	2	0.16	0.19
$\boldsymbol{\alpha_2}$	46.4	4	2	0.18	0.21
$\boldsymbol{\beta_1}$	479	2	2	0.92	2.18
$\boldsymbol{\beta_2}$	505	2	2	0.98	2.31
$\boldsymbol{\gamma_1}$	840	2	2	1.62	3.83
$\boldsymbol{\gamma_2}$	882	2	2	1.70	4.05
$\boldsymbol{\eta_1}$	1846	1	2	1.79	8.43
$\boldsymbol{\eta_2}$	2059	1	2	1.99	9.41

References

1. Huang, Y. *et al.* Universal mechanical exfoliation of large-area 2D crystals. *Nat. Commun.* **11**, 2453 (2020).

2. Velický, M. *et al.* Mechanism of Gold-Assisted Exfoliation of Centimeter-Sized Transition-Metal Dichalcogenide Monolayers. *ACS Nano* **12**, 10463–10472 (2018).

3. Shiming, L. *et al.* High mobility in a van der Waals layered antiferromagnetic metal. *Sci. Adv.* **6**, 6407 (2020).

4. Dalgaard, K. J. *et al.* Anomalous Shubnikov-de Haas quantum oscillations in $NdTe_3$. *Phys. Rev. B.* **102**, 245109 (2020).

5. Novoselov, K. S. *et al.* Two-dimensional gas of massless Dirac fermions in graphene. *Nature* **438**, 197–200 (2005).

6. Anisimov, V. I., Zaanen, J and Andersen, O. K. Band Theory and Mott insulators:Hubbard *U* instead of Stoner *I*. *Phys. Rev. B* **44**, 943 (1991).

7. Anisimov, V. I. *et al.,* Density functional theory and NiO photoemission spectra. *Phys. Rev. B* **48**, 16929 (1993).

8. Aryasetiawan, F. *et al.,* Frequency-dependent local interactions and low-energy effective models from electronic structure calculations. *Phys. Rev. B* **70**, 195104 (2004).

9. Kresse, G. and Furthmüller, J. Efficiency of ab-initio total energy calculations for metals and semiconductors using a plane-wave basis set, *Comp. Mat. Sci.* **6**, 15 (1996).

10. Kresse, G. and Furthmüller, J. Efficient iterative schemes for ab-initio total-energy calculations using a plane-wave basis set, *Phys. Rev. B* **54**, 11169 (1996).

11. Kaltak, M. Merging GW with DMFT. *PhD Thesis, University of Vienna* (2015).

12. Hartstein, M. *et al.* Fermi surface in the absence of a Fermi liquid in the Kondo insulator SmB_6. *Nat. Phys.* **14**, 166-172 (2018) .

13. Lei, Z. *et al.* Gate-defined two-dimensional hole and electron systems in undoped InSb quantum well. *ArXiv:2208-10427* (2022).

14. Hartstein, M. *et al.* Intrinsic bulk quantum oscillations in a bulk unconventional insulator SmB_6. *iScience* **23**, 101632 (2020).

15. Walmsley, P. *et al.* Magnetic breakdown and charge density wave formation: A quantum oscillation study of the rare-earth tritellurides. *Phys. Rev.* B **102**, 045150 (2020).

16. Sakamoto, I. *et al.* de Haas-van Alphen effect in ytterbium and uranium compounds. *J. Alloys Compd.* **275-277**, 505-509 (1998).

17. Ru, N. *et al.* de Haas-van Alphen oscillations in the charge density wave compound lanthanum tritelluride $LaTe_3$. *Phys. Rev. B* **78**, 045123 (2008).

18. Kumar, N. *et al.* Extremely high conductivity observed in the triple point topological metal MoP. *Nat. Commun.* **10**, 2475 (2019).

19. Schönemann, R. Fermi surface of Weyl type-II metallic candidate WP_2. *Phys. Rev. B* **96**, 121108(R) (2017).

20. Uchida, M. *at al.* Quantum Hall states observed in thin films of Dirac semimetal Cd_3As_2. *Nat. Commun.* **8**, 2274 (2017).

21. Xu, C. Q. *et al.* Enhanced electron correlations in the binary stannide $PdSn_4$ homologue of the Dirac nodal arc semimetal $PtSn_4$. *Phys. Rev. Materials* **1**, 064201 (2017).

22. Liu, H. *et al.* f-electron hybridised Fermi surface in magnetic field-induced metallic YbB_{12}. *npj Quantum Mater.* **7**, 12 (2022).

23. Mun, E. *et al.* Magnetic field effects on transport properties of $PtSn_4$. *Phys. Rev. B* **86**, 035135 (2012).

24. McCollam, A. Quantum oscillations and subband properties of the two-dimensional electron gas at the $LaAlO_3/SrTiO_3$ interface. *Appl. Phys. Lett.* **2**, 022102 (2014).

25. Liu, Y. *et al.* Zeeman splitting and dynamical mass generation in Dirac semimetal $ZrTe_5$. *Nat. Commun.* **7**, 12516 (2016).